Lawrence Berkeley National Laboratory
LBL Publications

Title
Enhanced structural stability in Mn—rich layered transition metal oxide positive electrode materials via germanium substitution

Permalink
https://escholarship.org/uc/item/4p22z9nt

Journal
Energy Storage Materials, 90

ISSN
2405-8297

Authors
Hu, Jiacheng
Deng, Shuolei
Gabriel, Eric
et al.

Publication Date
2026-08-01

DOI
10.1016/j.ensm.2026.105399

Copyright Information
This work is made available under the terms of a Creative Commons Attribution License, available at https://creativecommons.org/licenses/by/4.0/

Peer reviewed

eScholarship.org Powered by the California Digital Library
University of California

Energy Storage Materials 90 (2026) 105399

Contents lists available at ScienceDirect

Energy Storage Materials

journal homepage: www.elsevier.com/locate/ensm

Enhanced structural stability in Mn–rich layered transition metal oxide positive electrode materials via germanium substitution

Jiacheng Hu [a,1], Shuolei Deng [a,1], Eric Gabriel [a], Gi–Hyeok Lee [b], Yongkang Jin [c,d], Wanli Yang [b], Yan–Yan Hu [c,d], Blake Michaelsen [a], Chengjun Sun [e], Andrey Yakovenko [e], Jue Liu [f], Sarah Pooley [a], Joshua A. Russell [a], Cyrus Koroni [a], Kincaid Graff [a], Darin Schwartz [g], Shelly Kelly [e], Yifan Dong [a,*], Hui Xiong [a,*]

[a] Micron School of Materials Science and Engineering, Boise State University, Boise, ID, 83720, USA
[b] Advanced Light Source, Lawrence Berkeley National Laboratory, Berkeley, CA, 94720, USA
[c] Department of Chemistry and Biochemistry, Florida State University, Tallahassee, FL, 32306, USA
[d] Centre for Interdisciplinary Magnetic Resonance, National High Field Magnetic Laboratory, Tallahassee, FL, 32310, USA
[e] X–ray Science Division, Advanced Photon Source, Argonne National Laboratory, Lemont, IL, 60439, USA
[f] Neutron Scattering Division, Oak Ridge National Laboratory, Oak Ridge, TN, 37830, USA
[g] Department of Geosciences, Boise State University, Boise, ID, 83720, USA

ARTICLE INFO

Keywords:
Na–ion batteries
Positive electrode materials
Layered oxides
Structural stability
Ge substitution

ABSTRACT

Manganese–rich layered oxides are among the most promising positive electrode candidates for sodium–ion batteries due to their abundant resources and relatively high theoretical specific capacity. However, conventional P2–type layered transition metal oxides suffer from structural instability, particularly at high voltages, resulting in poor capacity retention. Here, we investigate the effect of Ge substitution on the structural and electrochemical properties of $Na_{0.67}Ni_{0.33}Mn_{0.67}O_2$ at high voltage. X–ray and neutron diffraction analyses reveal that the P2 phase and honeycomb ordering are preserved after Ge^{4+} substitution. Meanwhile, the enlarged sodium layer spacing facilitates Na^+ diffusion, enhancing ionic transport and transfer kinetics, which leads to improved rate capability. Particularly, $Na_{0.67}Ni_{0.33}Mn_{0.62}Ge_{0.05}O_2$ (NNMO–$Ge_{0.05}$) exhibits a high–rate capability and excellent cycling stability, retaining 81% of its capacity after 500 cycles at 150 mA g^{-1} between 2 - 4.2 V, compared with the undoped sample (69%). Moreover, it also shows excellent electrochemical performance among recently reported NNMO–based materials. ^{23}Na solid–state nuclear magnetic resonance and *operando* synchrotron X–ray diffraction characterizations demonstrate that the enhanced performance arises from stabilization of the P2 phase and suppression of the detrimental O2 phase at high voltage. Soft X–ray TM *L*–edge absorption spectroscopy and O *K*–edge resonant inelastic X–ray scattering analyses suggest that charge compensation is predominantly governed by reversible Ni redox, with limited direct participation of lattice oxygen. This work provides a simple and effective strategy for improving the performance of Mn–rich layered transition metal oxide positive electrode materials through Ge substitution.

1. Introduction

With the rapid expansion of electric vehicles and smart grids, sodium ion batteries (SIBs) have emerged as a promising complement to lithium–ion batteries (LIBs) due to the natural abundance and low–cost of sodium resources [1,2]. However, Na exhibits a higher electrode potential than Li (−2.714 V for Na, −3.045 V for Li) and a larger ionic radius (1.02 Å), which leads to a lower energy density and sometimes sluggish Na^+ transport kinetics, hindering the practical application of SIBs. Consequently, the development of advanced positive electrode materials with high capacity, robust cycling stability, and fast Na^+ diffusion has become a critical research priority [3]. Among various candidates, P2–type $Na_{0.67}Ni_{0.33}Mn_{0.67}O_2$ (NNMO) positive electrode material has attracted significant attention owing to its high working

* Corresponding authors.
E-mail addresses: dyfdongyifan@gmail.com (Y. Dong), clairexiong@boisestate.edu (H. Xiong).
[1] These authors contributed equally to this work.

https://doi.org/10.1016/j.ensm.2026.105399
Received 17 April 2026; Received in revised form 9 July 2026; Accepted 18 July 2026
Available online 19 July 2026
2405-8297/© 2026 The Author(s). Published by Elsevier B.V. This is an open access article under the CC BY-NC license (http://creativecommons.org/licenses/by-nc/4.0/).

voltage (~3.7 V), relatively high energy density, and good air stability [4]. Nevertheless, NNMO suffers from several issues under high–voltage operation, including anisotropic lattice distortion, irreversible P2–O2 phase transitions, irreversible oxygen redox associated with gas evolution, and parasitic surface reactions [4,5]. Addressing these issues is essential for realizing high–performance sodium–ion batteries.

To tackle the issues at high–voltage operation for NNMO, several strategies have been employed, including surface coating [6] and elemental substitution [7,8]. Liu et al. demonstrated improved electrolyte stability when NNMO was coated with alumina by wet chemistry method [9], leading to improved capacity retention (achieved to 73.2% from 26.8% after 300 cycles between 2.5 – 4.3 V) and rate performance. However, the unfavorable P2–O2 phase transition still persisted, leading to exfoliation of layers. Elemental substitution, including electrochemically active cations (e.g., Cu^{2+}, Co^{2+}), nonactive cations (e.g., Li^{+}, Mg^{2+}, Zn^{2+}, Al^{3+}, Y^{3+}, Ti^{4+}, Nb^{5+}, W^{6+}) and anions (e.g., F^{-}), has been widely demonstrated to optimize the intrinsic structure by modulating bond energies, lattice parameters, and surface/interface properties, thereby enhancing structural and chemical stability [10]. Wu et al. [11] reported that high–valence W^{6+} effectively suppresses the P2–O2 phase transition in $Na_{0.67}Ni_{0.33}Mn_{0.66}W_{0.01}O_2$ under 4.2 V high voltage operation, leading to significantly improved cycling stability (77.6% capacity retention after 1000 cycles at 10 C rate). W^{6+}(ionic radius 0.60 Å) possesses both a higher valence state and a larger ionic radius than Mn^{4+}(0.53 Å), the resulting stronger W–O bonding expands the lattice, suppresses lattice oxygen release, and consequently improves structural stability. Table S1 (Supplementary Information) summarizes recent single element doping in NNMO, which generally enhance capacity retention during prolonged high–voltage cycling by stabilizing the layered framework.

However, most previously reported substitutions, particularly electrochemically active cations (e.g., Cu^{2+}, Co^{2+}) and anions (e.g., F^{-}), tend to modify the TM redox chemistry or alter the TM–O covalency, often leading to trade–offs between structural stability and reversible capacity. In contrast, the isovalent Ge^{4+} substitution at the Mn site provides a fundamentally different stabilization mechanism that decouples structural robustness from redox perturbation. Specifically, because Ge^{4+} possesses the same valence state and a nearly identical ionic radius to Mn^{4+} (r = 0.53 Å) [12,13], its incorporation preserves local charge neutrality and minimizes lattice strain, thereby maintaining the integrity of the TM–O framework. Additionally, Ge substitution may influence the local electronic structure, which could be beneficial for electrochemical performance [14].

When monovalent, divalent, or trivalent nonactive dopants (e.g., Li^{+}, Mg^{2+}, Zn^{2+}, Al^{3+}, Y^{3+}) substitute at Mn site in NNMO, the initial oxidation state of Ni^{2+} will be increased to satisfy charge–compensation requirement. Based on this, the redox activity of nickel may partly be curtailed [15]. Tetravalent dopants such as Ti^{4+} have the same valance of Ge^{4+}, but their relatively larger ionic radii (r = 0.61 Å) and/or more bonding character can introduce local lattice strain and increased polarization [16]. Moreover, the substitution of Mn^{4+} by the much heavier higher–valence dopants (e.g., Nb^{5+}, W^{6+}) may reduce the achievable gravimetric energy density because their large atomic masses increase formula weight without proportionally contributing to reversible capacity [17]. Ge^{4+} preserves the Mn^{4+} valence state, similar atomic mass and avoids charge–compensation–induced lattice instability. Collectively, these effects enable a coupling of structural stabilization with charge balance, allowing cycling stability without sacrificing reversible capacity.

Previous studies in LIBs further prove the beneficial role of Ge incorporation. Zhao et al. [18]. reported a Ge–doped $LiNi_{0.6}Co_{0.2}Mn_{0.2}O_2$ material, that delivered an increased discharge capacity of 145.6 mAh g^{-1} at 5 C rate (1C = 180 mA g^{-1}) within 2.7–4.3 V, compared to 130.4 mAh g^{-1} for the undoped counterpart, along with a capacity retention of 91.1% after 100 cycles at 1 C. Similarly, Zhang et al. [19] synthesized the Ge doped $Li_3V_2(PO_4)_3$/C materials via a sol–gel method, achieving discharge capacities of 137.2mAh g^{-1}at 0.2C compared to 127.9 mAh $g^{-1}$of the undoped sample and 118.4 mAh g^{-1}at 5C (vs. 50.6 mAh g^{-1}) in the voltage range of 2–4.3 V. Despite these promising results, the mechanistic role of Ge substitution in NNMO positive electrode materials for sodium–ion batteries remains largely unexplored.

Here, we investigate the impact of selectively substituting Mn^{4+} with Ge^{4+} on the NNMO structural stability and electrochemical performance in the high voltage range of 2.0–4.2 V. The content of Ge^{4+} is systematic optimized. It was found the modified $Na_{0.67}Ni_{0.33}Mn_{0.62}Ge_{0.05}O_2$ (NNMO–$Ge_{0.05}$), delivers an initial capacity of 126.27 mAh g^{-1} at 15 mA g^{-1} within 2.0–4.2 V, representing a 21% improvement over the undoped NNMO of 103.87 mAh g^{-1}. Through integrated multi–scale ex– and in–situ characterizations (e.g., X–ray diffraction (XRD), neutron powder diffraction (NPD), scanning electron microscopy (SEM), transmission electron microscopy (TEM), x–ray absorption spectroscopy (XAS), ^{23}Na solid–state nuclear magnetic resonance (NMR)), we found Ge substitution suppresses P2–O2 phase transitions while broadening Na^{+} diffusion pathways, resulting in significantly improved cycling stability and rate capability. This work presents a promising strategy for developing high–capacity, stable P2–type layered oxide positive electrode materials, offering valuable design insights for the development of high–performance positive electrode materials for SIBs.

2. Results and discussion

2.1. Structure and morphology

Ge–substituted P2–type $Na_{0.67}Ni_{0.33}Mn_{0.67-x}Ge_xO_2$ (NNMO–Ge_x, x = 0, 0.02, 0.05, 0.10) were synthesized via simple solid–state reaction [20]. Inductively coupled plasma mass spectrometry (ICP–MS) analysis confirmed that the chemical composition of the as–prepared samples is consistent with the expected stoichiometry (Table S2, Supplementary Information). Fig. 1a shows the powder X–ray diffraction (XRD) result of the four as–prepared samples. All samples exhibit a P2–type layered structure (space group $P6_3/mmc$), with only trace amounts of Na_2GeO_3 phase detected at Ge contents above x > 0.05 (Fig. 1a). In order to better investigate the lattice changes (Fig. 1b) induced by Ge substitution, the crystal structures of NNMO–Ge_x were further analyzed by Rietveld refinement of the XRD data [21], which are shown in Fig. 1c, 1d and S1 (Supplementary Information). The refined lattice parameters for NNMO are $a = b = 2.8839(1)$ Å, $c = 11.1506(2)$ Å, and $V = 80.314(3)$ Å^3 (Table S3, Supplementary Information). Increasing the Ge content causes c and corresponding volume to gradually increase (Fig. 1b), suggesting Ge substitution can facilitate enlarged diffusion pathways for Na^{+} migration with lower Na^{+} diffusion barriers. On the other hand, the *ab* plane contracts with increased Ge content (Figure S2, Supplementary Information). The schematic illustration of the changes of crystal structures after Ge substitution is shown in Figure S3 (Supplementary Information). It is postulated that the changes in lattice parameters may be associated with the unique [Ar]$3d^{10}$ electron configuration of Ge^{4+} (Figure S4, Supplementary Information). Ge^{4+} has nearly identical ionic radius (r = 0.53 Å) as Mn^{4+} ([Ar]$3d^3$), allowing it to easily substitute for Mn without disrupting the honeycomb cation–ordered structure of P2–NNMO [22]. Neutron powder diffraction (NPD) confirms that the TM ordering with ABAB stacking of Ni and Mn/Ge remains after Ge substitution (Fig. 1e and 1f), according to the good fit of the indexed peaks to the $P6_3$ space group [23]. However, the completely filled d–orbitals of Ge^{4+} cannot accommodate the typical TM 3d–O 2p hybridization of layered oxides and instead bond via the empty 4s/4p Ge orbitals. This is expected to have substantial effects on the local electronic structure of oxygen and coordinating transition metal elements.

The morphology and microstructure of the as–prepared NNMO–$Ge_{0.05}$ were characterized by scanning electron microscopy (SEM) and high–resolution transmission electron microscopy (HRTEM). The sample exhibits a plate–like morphology with an average particle

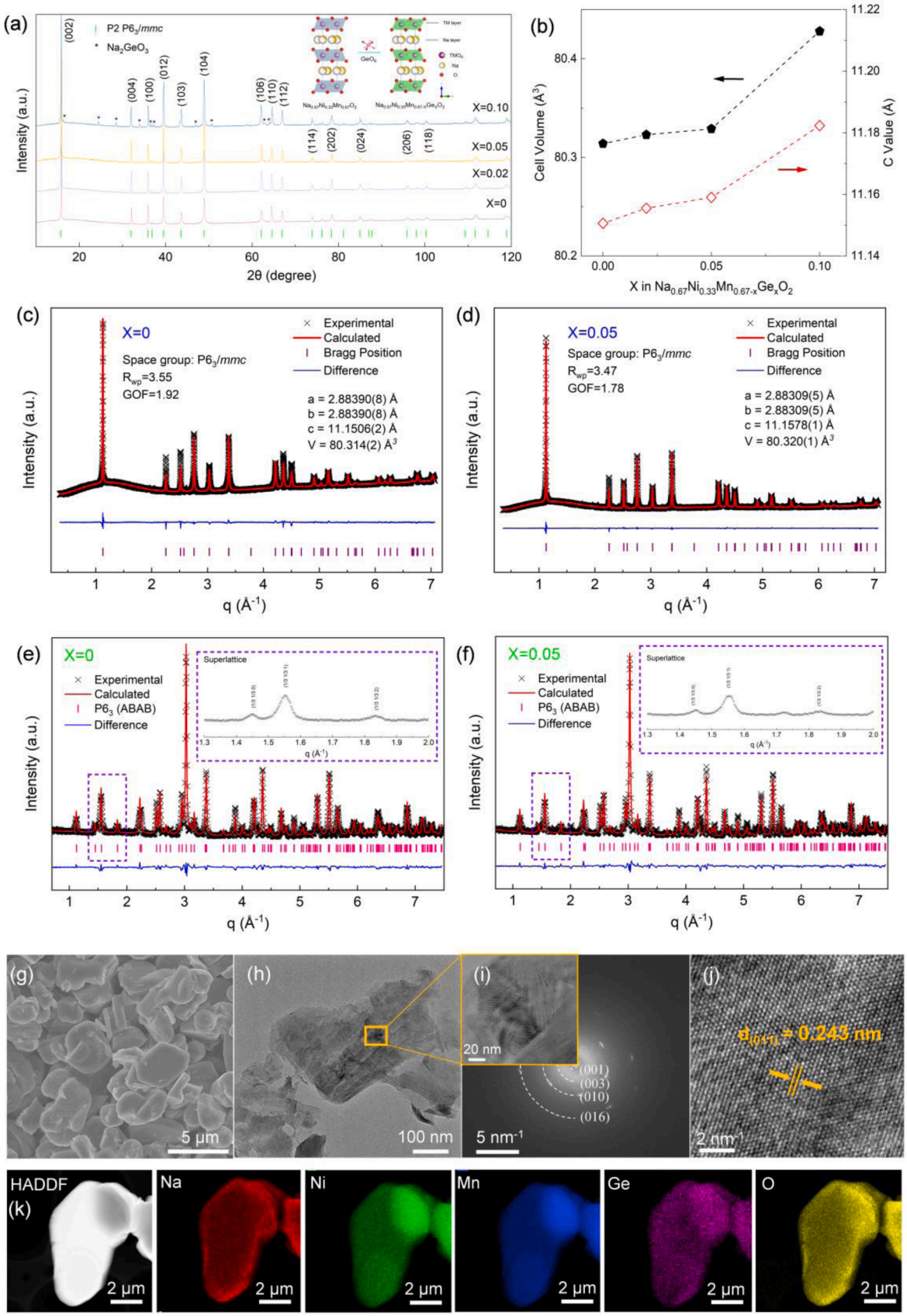


Fig. 1. Structure characterization. (a) Experimental PXRD patterns of NNMO–Ge_x, inset: the schematic illustration of the changes of crystal structures after Ge substitution; (b) The changes of c and volume values with the Ge substituting increases after refinement; The Rietveld refinement of PXRD and NPD patterns of (c, e) NNMO and (d, f) NNMO–$Ge_{0.05}$; Inset: intralayer ordering; (g) The SEM, (h) TEM, (i) HRTEM (inset) and SAED patterns of the NNMO–$Ge_{0.05}$ sample; (j) HRTEM image along the (011) zone axis; (k) HAADF and corresponding EDS mapping images of NNMO–$Ge_{0.05}$.

size of approximately 3 μm (Fig. 1g). The HRTEM image and the corresponding fast Fourier transform (FFT) image reveal lattice resolved fringes with a spacing of 0.243 nm, corresponding to the (011) plane of the P2–type hexagonal system (Fig. 1h–1j). The high–angle annular dark–field (HAADF) and combined energy–dispersive spectroscopy (EDS) mappings (Fig. 1k) demonstrate the uniform distribution of Na, Ni, Mn, Ge, and O elements in NNMO–$Ge_{0.05}$.

2.2. Electrochemical properties

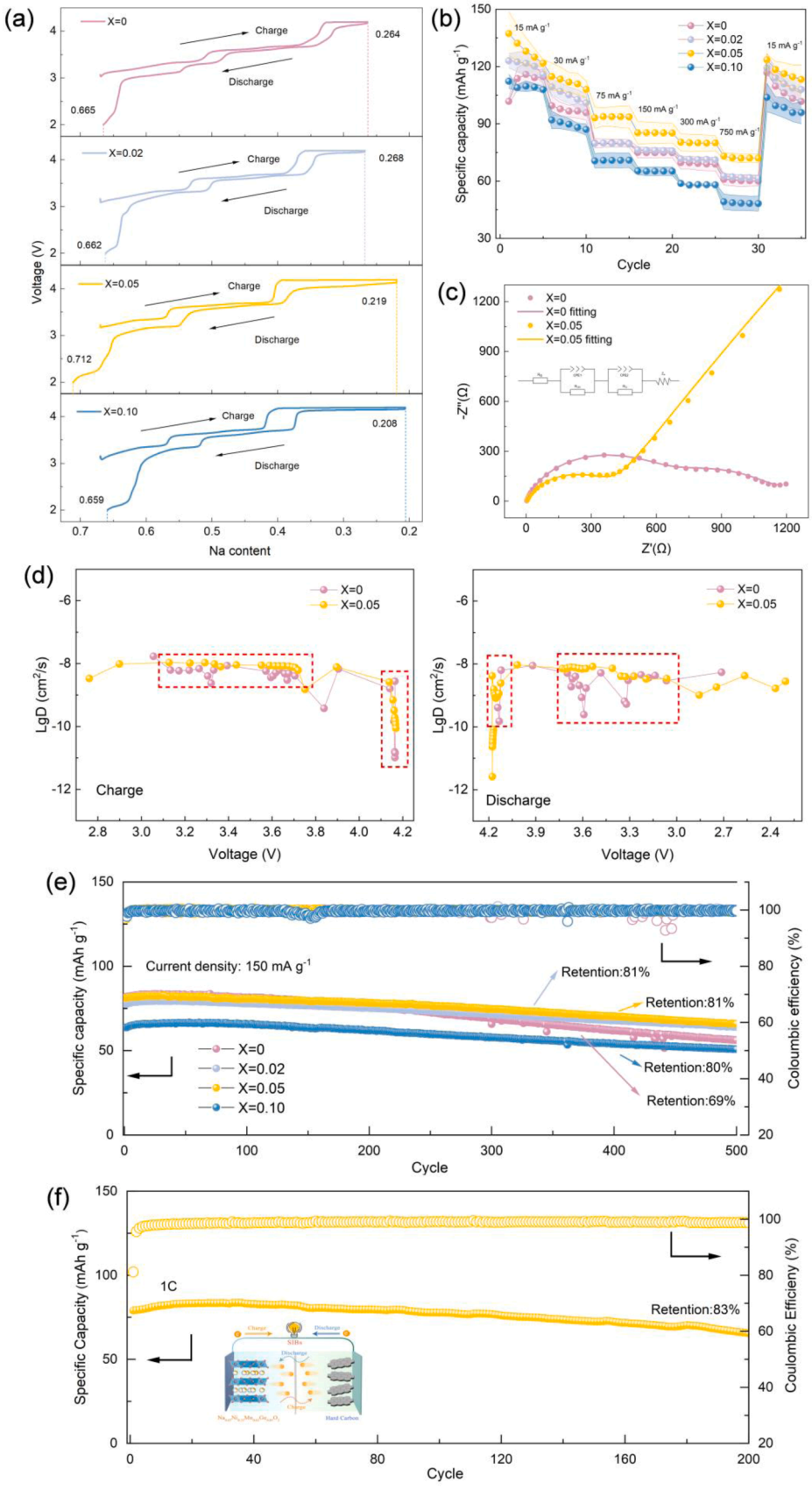
The electrochemical properties of NNMO–Ge_x were assessed in coin–type sodium half cells in the voltage range of 2–4.2 V (vs Na/Na^+). All measurements were conducted for at least three duplicates, and the averaged values with standard deviations are included in Fig. 2, confirming the excellent reproducibility of the electrochemical performance. Three plateaus at ~3.3, ~3.7, and ~4.2 V were observed during the first charge, which are in agreement with those reported in the literature [7]. The first–cycle charge/discharge curves of NNMO–Ge_x are shown in Fig. 2a and Figure S5 (Supplementary Information), exhibiting an initial charge/discharge capacity of 105.06/103.87 mAh g^{-1} for NNMO, 103.82/101.77 mAh g^{-1} for NNMO–$Ge_{0.02}$, 115.63/126.27 mAh g^{-1} for NNMO–$Ge_{0.05}$, and 118.05/115.29 mAh g^{-1} for NNMO–$Ge_{0.10}$ at 15 mA g^{-1} between 2-4.2V. There is little difference in initial charge/-discharge capacity among the NNMO and NNMO–$Ge_{0.02}$ samples, indicating that 2% Ge substitution has no obvious effect on the initial performance of NNMO. However, with increasing Ge content, the voltage plateau at 4.2 V during charge extends, resulting in an increase in the capacity of the material. The extended plateau of NNMO–$Ge_{0.05}$ and NNMO–$Ge_{0.10}$ may be associated with a stabilized single P2 framework and the formation of O–type stacking faults, which is supported by *Operando* XRD results discussed later. While local stacking faults with O–type character may be introduced by substitution and help accommodate structural strain, they do not correspond to a bulk phase transformation but instead contribute to maintaining structural integrity and reversibility. This improvement is also associated with the expanded Na interlayer spacing due to Ge substituting, which regulates interlayer electrostatic repulsion between TMs, thereby enabling more reversible Na^+ extraction at high voltage. The increased discharge capacity in NNMO–$Ge_{0.05}$ is partially associated with enhanced Na insertion at low voltage, involving additional Na^+ occupation of Na/vacancy–ordered sites and accompanying Mn^{4+}/Mn^{3+} redox (Fig. 3b and 3e). The Columbic efficiency of the NNMO–$Ge_{0.05}$ electrode becomes 97.9% and 98.2% in the second and third cycles, respectively (Figure S6, Supplementary Information), indicating that the electrode stabilizes after the initial cycle, with minimal irreversible reactions. The decreased capacity in NNMO–$Ge_{0.10}$ compared to NNMO–$Ge_{0.05}$ might be associated with the existance of the inactive Na_2GeO_3 phase in the sample. In addition, NNMO–$Ge_{0.05}$ exhibits the highest reversible capacity (70.69 mAh g^{-1}) after 100 cycles at 150 mA g^{-1} among the four samples (Figure S7, Supplementary Information), indicating that its structure remains more stable during long–term cycling. The rate capability of the four samples is shown in Fig. 2b. NNMO shows a significant decrease in discharge specific capacity with increasing current density, declining to 60.2 mAh g^{-1} at 750 mA g^{-1}. In contrast, NNMO–$Ge_{0.02}$ and NNMO–$Ge_{0.05}$ exhibit higher specific capacities at 750 mA g^{-1}, while NNMO–$Ge_{0.10}$ does not possibly due to the Na_2GeO_3 phase present. When the current density is increased from 15 to 750 mA g^{-1}, the reversible capacities of NNMO–$Ge_{0.05}$ are 127.9, 111.8, 93.7, 85.3, 80.0 and 71.9 mAh g^{-1}, respectively. Upon returning the current density to 15 mA g^{-1}, the reversible capacity of NNMO–$Ge_{0.05}$ reaches 116.2 mAh g^{-1}, retaining 91% of the initial capacity. These results demonstrate the excellent reversibility of Na^+ transport, which is attributed to the larger "Na layer distance ($d_{O—Na–O}$)" of NNMO–$Ge_{0.05}$ (Figure S3, Supplementary Information).

The electrochemical impedance spectroscopy (EIS) measurements were performed on NNMO and NNMO–$Ge_{0.05}$ materials at pristine state to investigate their kinetic behavior [24]. The impedance spectra, equivalent circuit model, and the fitted results are shown in Fig. 2c and Table S9 (Supplementary Information). Both materials exhibit one small semicircle near the high frequency region, one larger semicircle in the intermediate frequency region, and an inclined line in the low frequency region. These features correspond to the ohmic resistance of the electrode material (R_Ω) at the intercept, electrode/electrolyte interfacial resistance (R_{CEI}), charge transfer resistance (R_{ct}), and Warburg impedance (Z_w). The R_{ct} is associated with Na^+charge transfer resistance at the interface between the electrode and the electrolyte [25]. It is observed that the pristine NNMO electrode exhibited apparently higher R_{ct} (221.5 Ω) values than those of NNMO–$Ge_{0.05}$ (152.5 Ω; in Table S9, Supplementary Information), indicating enhanced interfacial redox kinetics. This improvement is attributed to the stabilized Mn/Ge–O framework and reduced structural polarization during Na extraction/insertion (Fig. 3a and 3b). Galvanostatic intermittent titration technique (GITT) studies were completed in Fig. 2d, it can be seen at ~3.3, ~3.7 and ~4.2 V the diffusion coefficient for the NNMO–$Ge_{0.05}$ is far more stable through the voltage window and larger compared to the undoped NNMO sample especially on the discharge, indicating a better kinetic for NNMO–$Ge_{0.05}$ electrode. The reduced charge–transfer resistance together with the enhanced Na^+ diffusion coefficient derived from GITT collectively demonstrate that Ge^{4+} substitution accelerates both interfacial redox kinetics and bulk charge transport, leading to globally improved electrochemical kinetics. This also supports the cyclic voltammetry (CV) results (Fig. 3a and 3b).

In addition, the cycling performance of these samples under a current density of 150 mA g^{-1} in half cells is compared in Fig. 2e, NNMO–$Ge_{0.05}$ exhibits excellent cycling stability, possessing a capacity retention of ~81% after 500 cycles (65.9 mAh g^{-1}), compared to NNMO (69%, 56.2 mAh g^{-1}), NNMO–$Ge_{0.02}$ (81%, 64 mAh g^{-1}), and NNMO–$Ge_{0.1}$ (80%, 50.8 mAh g^{-1}). Furthermore, it also exhibits superior cycling performance compared with previously reported NNMO–based positive electrode materials, as illustrated in Figure S8 (Supplementary Information). Besides, NNMO–$Ge_{0.05}$ exhibits a more stable average discharge voltage during prolonged cycling (Figure S9, Supplementary Information), with only 3.6% voltage decay, compared to NNMO (5.9%), NNMO–$Ge_{0.02}$ (4.4%) and NNMO–$Ge_{0.10}$ (5.4%), indicating suppressed voltage fading and improved electrochemical reversibility. Furthermore, a coin–type full cell comprising the NNMO–$Ge_{0.05}$ positive and commercial hard carbon (HC) negative electrode material (denoted as NNMO–$Ge_{0.05}$//HC) was assembled (Figure S10, Supplementary Information) to evaluate the practical applicability of NNMO–$Ge_{0.05}$ material. As shown in Fig. 2f, the NNMO–$Ge_{0.05}$//HC full cell delivers a excellent cycling stability, retaining ~83% after 200 cycles at a 1C rate and the energy density of full cell is 294 Wh kg^{-1} at a power density of 35 W kg^{-1} based on the active mass of the positive and negative electrode materials. These results highlight the potential of Ge–substituted NNMO for practical sodium–ion full cells. The current loading density of the positive electrode material is about 2.8 mg/cm^2 and it could be engineered to achieve high loading density for pouch cell configuration for future improvement.

2.3. Redox behaviors

Cyclic voltammetry (CV) measurements were conducted at a scan rate of 0.1 mV s^{-1} and six peak pairs (centered at 2.35/2.27, 3.26/2.98, 3.37/3.29, 3.64/3.56, 3.71/3.64 and 4.2/4.12 V) are discerned in NNMO (Fig. 3a). The peaks below 3 V are associated with Mn^{3+}/Mn^{4+} redox. The redox peaks around ~3.3 V and ~3.7 V correspond to the $Ni^{2+}/Ni^{3+}/Ni^{4+}$ redox and Na^+/vacancy ordering rearrangement in the sodium layer, while peaks around 4.2 V is associated with the P2–O2 transition and oxygen redox [26,27]. CV curves of NNMO electrode show a significant voltage hysteresis at 4.1 V, suggesting irreversible structural evolution within the first 3 cycles. It is noteworthy that with Ge^{4+} substitution, the curves are broader, smoother and more



(caption on next page)

Fig. 2. Electrochemical properties: (a) Galvanostatic charge–discharge voltage profiles of electrodes of the first cycle at 15 mA g^{-1} within 2.0–4.2 V; (b) Rate capability. The error band represents the standard deviation between multiple cells of the sample; (c) Nyquist plots of pristine NNMO and NNMO–$Ge_{0.05}$ electrode materials; (d) The comparation of GITT of NNMO and NNMO–$Ge_{0.05}$ at charge and discharge state; (e) Cycling performance of NNMO–$Ge_{0.05}$ at 150 mA g^{-1} in comparison with the NNMO, NNMO–$Ge_{0.02}$ and NNMO–$Ge_{0.1}$ counterparts; (f) Cycling performance of a coin–type NNMO–$Ge_{0.05}$//hard carbon full cell at 1C rate within 1.9–4.1 V (capacity based on the active mass of the positive electrode); Inset: schematic diagram of the full cell with NNMO–$Ge_{0.05}$ and hard carbon electrode material.

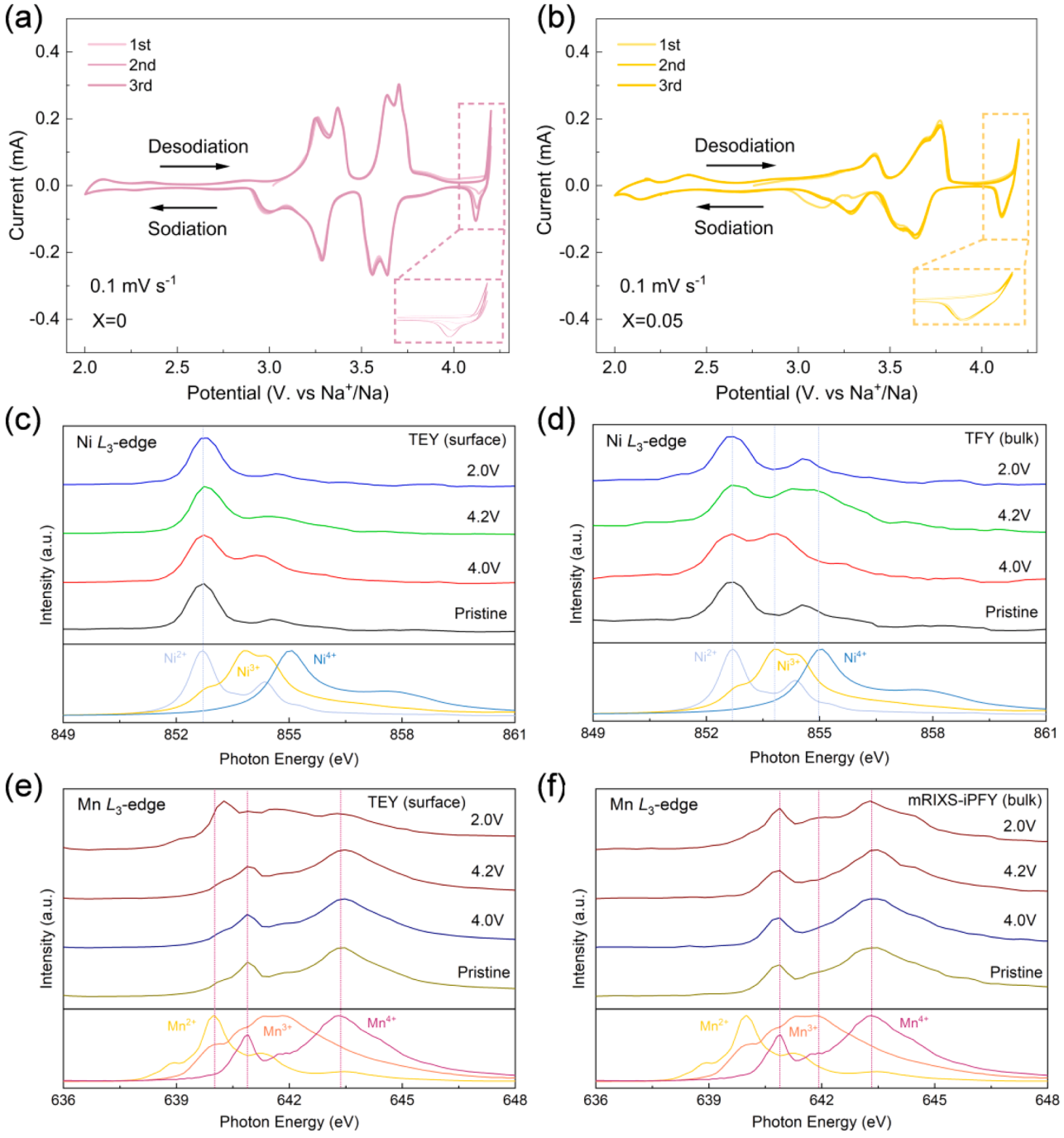


Fig. 3. TM Redox behavior analyses based on X–ray absorption spectroscopy: CV curves of (a) NNMO and (b) NNMO–$Ge_{0.05}$ in initial three cycles at a scan rate of 0.1 mV s^{-1}; Ex–situ (c) surface and (d) bulk Ni and (e) surface and (f) bulk Mn L_3–edge sXAS spectra of NNMO–$Ge_{0.05}$ at different SOCs.

reversible, and the intensity of the redox peak corresponding to the $Ni^{3+/}Ni^{4+}$ redox at ~4.2 V gradually stabilizes (Fig. 3b). This suggests that Ge^{4+} substitution effectively enhances the stability of the material's crystal structure by suppressing the P2–O2 phase transition, thereby effectively increasing the reversibility. The suppressed phase transition and oxygen redox were directly confirmed by operando XRD and O *K*–edge mapping of resonant inelastic X–ray scattering (mRIXS) analysis discussed later.

The aforementioned scenario is confirmed by a series of spectroscopic characterizations for probing the valence states of all relevant

elements in NNMO–$Ge_{0.05}$ at different states of charge. First, soft X–ray TM *L*–edge absorption spectroscopy (sXAS) (Fig. 3c–f) directly probes the 3*d* valence states through the *2p–3d* excitations. Two different probe depths of about 10 and 100–200 nm could be achieved through the total electron yield (TEY) and total fluorescence yield (TFY) mode, respectively [28]. We measured Ni–L_3 edge TEY (surface, Fig. 3c) and TFY (bulk, Fig. 3d) sXAS with reference spectra for direct comparison. For Mn, conventional TFY is known to suffer serious distortion in lineshape due to the abrupt change in penetration depth at the absorption edge [29], so we employed inverse partial fluorescence yield (iPFY; bulk) extracted from mRIXS to evaluate the bulk Mn valence states [29]. Fig. 3c and 3d show the oxidation state evolution of Ni in NNMO–$Ge_{0.05}$ during the charge/discharge process at the first cycle. The pristine state displays a sharp peak at ~853 eV and a hump at ~855 eV, which mainly corresponds to the Ni^{2+}, consistent with the hard XAS results (Figure S11, Supplementary Information) and previous results [30,31]. When the electrode is charged to 4.0 V, the relative peak intensity at ~854 eV for Ni^{3+} increases, suggesting that the $Ni^{2+/3+}$ redox contributes to the charge compensation in the bulk of the electrode, with further oxidation toward a mixed $Ni^{3+/4+}$ state at 4.2 V. Upon discharge to 2.0 V, the spectral features largely recover toward the pristine state, indicating a predominantly reversible Ni redox process. Fig. 3e and 3f show the Mn L_3–edge TEY (surface) and mRIXS–iPFY (bulk) compared with references. In the bulk, as expected, Mn maintains Mn^{4+}, indicating Mn is an inactive redox component. It is important to note that, through such a comparative surface versus bulk study, we found a finite amount of Mn reduction to Mn^{3+} in the bulk, but clear evidence of Mn reduction to Mn^{2+} on the surface when the electrode is discharged to 2.0 V.

We further characterized the oxygen state evolution to the high voltage through O *K*–edge RIXS (Figure S12, Supplementary Information). A feature in the O–*K* RIXS map at an excitation energy of 531.2 eV is characteristic of oxidized oxygen dimerization [32]. But O–*K* RIXS maps of pristine and 4.2 V charged NNMO–$Ge_{0.05}$ show no such pronounced feature, indicating the oxygen oxidation towards dimerization has not been observed in NNMO–$Ge_{0.05}$.

The analysis of the ex–situ soft X–ray studies above is further confirmed by *Operando* hard X–ray absorption near–edge structure (XANES) measurements of NNMO–$Ge_{0.05}$ conducted at TMs *K*–edge (Figure S11, Supplementary Information). It shows that the Ni and Mn is mainly in the 2+ and 4+ state in NNMO and NNMO–$Ge_{0.05}$ samples at pristine state (Figure S11a and S11b, Supplementary Information), which is consistent with the sXAS results (Fig. 3c and 3d). The edge of Ni *K*–edge XANES (Figure S11c, Supplementary Information) in NNMO–$Ge_{0.05}$ shifts to higher energy during charging process and then returns to the lower energy region when discharged to 2 V, indicating both oxidation and reduction of Ni occurs upon charging and discharging. The edge positions of the Mn *K*–edge XANES spectra (Figure S11d, Supplementary Information) undergo negligible shifts during the charge/discharge process, indicating that the valence of Mn remains essentially unchanged. Although Mn *K*–edge hXAS indicates an overall electrochemically inactive Mn framework, the Mn L_3–edge in sXAS (both in TEY and iPFY) reveals a very minor Mn^{4+} to Mn^{3+} reduction at ~2 V, suggesting a localized and non–dominant Mn redox contribution that is likely confined to near–surface or defect regions [33]. Combined Ni/Mn L_3– and *K*–edge XAS and O *K*–edge RIXS analyses demonstrate that the electrochemical charge compensation in NNMO–$Ge_{0.05}$ is predominantly governed by a reversible bulk $Ni^{2+}/Ni^{3+}/Ni^{4+}$redox process, while Mn largely remains electrochemically inactive at bulk scale. No clear spectroscopic signatures of oxidized oxygen dimerization are observed, indicating that lattice oxygen does not participate directly in charge compensation. Overall, NNMO–$Ge_{0.05}$ has a stable electronic structure at high voltage and shows a highly reversible, cation–dominated charge compensation mechanism.

2.4. Structural evolution

Fig. 4a, 4b and S13 (Supplementary Information) compare the high–resolution ^{23}Na NMR spectra of NNMO and NNMO–$Ge_{0.05}$, obtained via the advanced pj–MATPASS (pj = projection, MAT = magic–angle turning, PASS = phase–adjusted sideband separation) method [34,35]. The downfield resonances between 1250–2000 ppm correspond to Na sites in the primary P2 phase, where paramagnetic shifts arise from hyperfine interactions with neighboring transition metal ions. In the P2 structure, Na occupies both edge–sharing and face–sharing prismatic sites, which experience different hyperfine coupling strengths due to their distinct local TM coordination environments. Na sites with a higher number of neighboring TM ions, particularly those coordinated with stronger TM–O covalency, are expected to exhibit more pronounced downfield shifts and broader resonances. Clusters of lower–intensity resonances within the 2000–1250 ppm range originate from Na environments with mixed Mn/Ni configurations in the first and second coordination shells. The upfield peaks around 0 ppm represent diamagnetic Na–containing phases, such as the unreacted Na residues from synthesis. Comparing the NNMO and NNMO–$Ge_{0.05}$, Ge doping increases the relative intensity of the primary (green shaded regions) P2 phase. The increased relative intensity contribution is attributed to a redistribution of local magnetic environments, where Na sites are more frequently surrounded by TM configurations with stronger and more uniform hyperfine coupling. Such changes may arise from modified altered TM–O covalency, and variations in the relative contributions of edge– and face–sharing Na sites induced by Ge substitution, collectively leading to an increased population of Na sites exhibiting larger paramagnetic shifts. In addition, Ge–substitution also leads to a reduced contribution from diamagnetic Na environments. To compare the long–range structural evolution and phase transition of NNMO and NNMO–$Ge_{0.05}$ during cycling, operando synchrotron XRD experiments were performed in Fig. 4c and 4d. Anisotropic lattice variation and P2–O2 phase transition (O2 phase around 1.5°) occur in the undoped NNMO sample during the first charge (Fig. 4c and Figure S14, Supplementary Information), which agrees with previous work [36]. Although the structural evolution appears to be reversible during the first charging–discharging process, the irreversible lattice deformations (such as generation of dislocations and slips) still exist. The considerable lattice mismatch between P2 and O2 phases introduces repetitive strain in the subsequent long–term cycling, causing detrimental lattice distortion or even micro–cracks within electrodes and eventually impairing the electrochemical performance [37] (Fig. 2c). In contrast, NNMO–$Ge_{0.05}$ does not undergo the P2–O2 phase transition throughout the first charge (Fig. 4c) based on the absence of the (002)' peak observed for undoped NNMO; instead, it only exhibits progressive peak shifts associated with lattice expansion/contraction during charging and discharging process and the formation of O–type stacking faults around 4.2 V, similar to previous work [38] (Figure S15, Supplementary Information). That suggests the structural stability improved with the Na^+ insertion/extraction. Moreover, during the discharge process, all the peaks return to their original position gradually, indicating the great reversibility of NNMO–$Ge_{0.05}$. In brief, through operando XRD analysis, the destructive P2-O2 phase transition in NNMO–$Ge_{0.05}$ is well suppressed and it shows better reversibility, which accounts for the enhanced structural stability and electrochemical performance.

3. Conclusion

In summary, we demonstrate Ge substitution (substituting for Mn in the TM layer) provides a viable approach for tuning the lattice parameters and suppressing phase transitions of NNMO. Operando sXRD reveals that the undoped NNMO undergoes a pronounced P2–O2 phase transition upon high–voltage charging, accompanied by abrupt lattice evolution and phase coexistence, indicative of severe structural instability. In contrast, strong Ge–O covalency introduced by Ge^{4+}

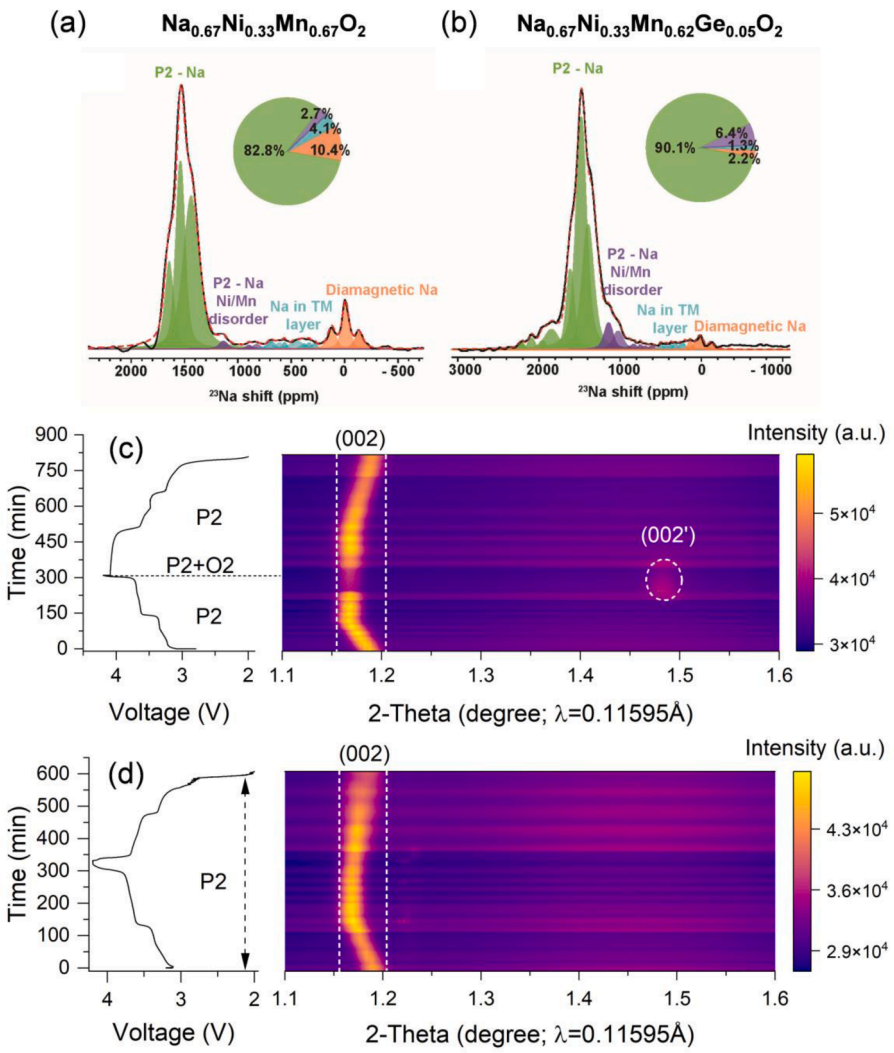


Fig. 4. Structural evolution: Processed 1D pj–MATPASS ^{23}Na NMR spectrum of (a) NNMO and (b) NNMO–$Ge_{0.05}$ and comparison of normal 1D MAS ^{23}Na NMR spectrum of NNMO and NNMO–$Ge_{0.05}$; In situ synchrotron XRD patterns obtained during the first galvanostatic charge/discharge cycle of (c) NNMO and (d) NNMO–$Ge_{0.05}$ at a current rate of 150 mA g^{-1} in the voltage range of 2–4.2 V.

substitution may help reinforce the TM–O framework and stabilize the oxygen sublattice, thereby suppressing slab gliding and mitigating the P2–O2 phase transition. The unique stabilizing effect of Ge^{4+} is hypothesized to result from its full [Ar]$3d^{10}$ orbital configuration, forming covalent Ge–O bonds on the Ge 4 s and 4p orbitals to stabilize lattice oxygen. Consequently, the TM–O framework becomes more rigid to resist the TMO_2 gliding that leads to undesired phase transitions [39, 40]. ^{23}Na NMR result further indicates that Ge doping increases the fraction of the primary P2 phase with modified altered TM–O covalency while reducing the amount of diamagnetic Na species. sXAS and hXAS reveal that the charge compensation in NNMO–$Ge_{0.05}$ is dominated by a highly reversible bulk $Ni^{2+}/Ni^{3+}/Ni^{4+}$redox process, with Mn remaining largely electrochemically inactive and no characteristic spectroscopic fingerprint of lattice oxygen redox was observed under the present experimental conditions. The strong coupling between stabilized Ni–centered charge compensation and suppressed layer gliding may contribute to the improved high–voltage stability of NNMO–$Ge_{0.05}$. As a result of this structural stabilization, NNMO–$Ge_{0.05}$ delivers markedly enhanced electrochemical performance, achieving 81% capacity retention at 150 mA g^{-1} after 500 cycles, compared to only 69% for undoped NNMO under identical conditions. And the NNMO–$Ge_{0.05}$//HC coin–type full cell further demonstrates durable cycling stability, maintaining ~98% and ~83% capacity retention after 100 and 200 cycles at 170 mA g^{-1}, respectively. Furthermore, our analyses unveil distinct redox behaviors between the surface and bulk, suggesting opportunities for further optimization through surface engineering or voltage regulation. More broadly, these findings suggest that combining structurally stabilizing dopants with redox–active or diffusion–regulating elements could provide a promising avenue for improving phase stability, redox reversibility, and Na^+ transport in layered oxide positive electrode materials. Moreover, the different surface and bulk redox behaviors revealed here imply that spatially resolved compositional engineering, such as surface–enriched stabilizing dopants coupled with redox–active bulk regions, may offer opportunities for simultaneously optimizing interfacial stability, reversible redox chemistry, and structural stability.

CRediT authorship contribution statement

Jiacheng Hu: Writing – review & editing, Writing – original draft, Visualization, Investigation, Formal analysis, Data curation. **Shuolei Deng:** Writing – original draft, Visualization, Formal analysis, Data curation. **Eric Gabriel:** Writing – review & editing, Formal analysis. **Gi–Hyeok Lee:** Writing – review & editing, Formal analysis, Data curation. **Yongkang Jin:** Writing – review & editing, Formal analysis, Data curation. **Wanli Yang:** Writing – review & editing, Formal analysis,

Data curation. **Yan–Yan Hu:** Writing – review & editing, Formal analysis. **Blake Michaelsen:** Data curation. **Chengjun Sun:** Data curation. **Andrey Yakovenko:** Data curation. **Jue Liu:** Data curation. **Sarah Pooley:** Investigation. **Joshua A. Russell:** Investigation. **Cyrus Koroni:** Writing – review & editing. **Kincaid Graff:** Writing – review & editing. **Darin Schwartz:** Data curation. **Shelly Kelly:** Data curation. **Yifan Dong:** Writing – review & editing, Writing – original draft, Data curation, Conceptualization. **Hui Xiong:** Writing – review & editing, Writing – original draft, Supervision, Resources, Project administration, Investigation, Funding acquisition, Formal analysis, Conceptualization.

Declaration of competing interest

The authors declare the following financial interests/personal relationships which may be considered as potential competing interests:

Hui Xiong reports financial support was provided by Department of the Navy, Office of Naval Research. Wanli Yang reports financial support was provided by US Department of Energy. If there are other authors, they declare that they have no known competing financial interests or personal relationships that could have appeared to influence the work reported in this paper.

Acknowledgement

This material is based upon work supported by the Department of the Navy, Office of Naval Research under Award Number N00014–23–1–2343. G.H.L. acknowledges the support from the U.S. Department of Energy, Office of Science, Office of Basic Energy Sciences program under Award Number DE–SC0024404. Soft X–ray experiments were performed at BL8.0.1.1 (iRIXS) of the Advanced Light Source (ALS), a DOE Office of Science User Facility, under contract No. DE–AC02–05CH11231. This research used beamline 11-ID-C and 20-BM of the Advanced Photon Source, a U.S. Department of Energy (DOE) Office of Science User Facility operated for the DOE Office of Science by Argonne National Laboratory under Contract No. DE-AC02-06CH11357. This research utilized the XRD, SEM, and TEM instruments in the Boise State University FaCT Core Facility, RRID: SCR_024733, which receives support from the National Institutes of Health [NIH] under the Institutional Development Awards [IDeA] Program of the National Institute of General Medical Sciences [NIGMS] via Grants P20GM148321 and P20GM103408. Funding for the analytical infrastructure of the Boise State Isotope Geology Laboratory used in this study was provided by NSF Grants EAR–1735889 and EAR–1920336.

Supplementary materials

Supplementary material associated with this article can be found, in the online version, at doi:10.1016/j.ensm.2026.105399.

Data availability

Data will be made available on request.

References

[1] Global EV Outlook 2024, Moving towards increased affordability, Int. Energy Agency (2024). https://www.iea.org/reports/global–ev–outlook–2024.
[2] Y. Gao, H. Zhang, J. Peng, L. Li, Y. Xiao, L. Li, Y. Liu, Y. Qiao, S. Chou, A 30–year overview of sodium–ion batteries, Carbon Energy 6 (2024) e464, https://doi.org/10.1002/cey2.464.
[3] L. Zhao, T. Zhang, W. Li, T. Li, L. Zhang, X. Zhang, Z. Wang, Engineering of sodium–ion batteries: opportunities and challenges, Engineering 24 (2023) 172–183, https://doi.org/10.1016/j.eng.2021.08.032.
[4] J. Zhang, W. Wang, W. Wang, S. Wang, B. Li, Comprehensive review of P2–type $Na_{2/3}Ni_{1/3}Mn_{2/3}O_2$, a potential cathode for practical application of Na–ion batteries, ACS. Appl. Mater. Interfaces. 11 (2019) 22051–22066, https://doi.org/10.1021/acsami.9b03937.
[5] D. Hou, E. Gabriel, K. Graff, T. Li, Y. Ren, Z. Wang, Y. Liu, H. Xiong, Thermal dynamics of P2–Na0.67Ni0.33Mn0.67O2 cathode materials for sodium ion batteries studied by in situ analysis, J. Mater. Res. 37 (2022) 1156–1163, https://doi.org/10.1557/s43578–022–00519–z.
[6] E. Gabriel, P. Wang, K. Graff, S.D. Kelly, C. Sun, C. Deng, I. Hwang, J. Liu, C. Li, S. Kuraitis, J. Park, E. Lee, A. Conrado, J. Pipkin, M. Cook, S. McCallum, Y. Xie, Z. Chen, K.M. Wiaderek, A. Yakovenko, Y. Ren, Y. Xiao, Y. Liu, E. Graugnard, Y.–Y. Hu, D. Hou, H. Xiong, The role of Li doping in layered/layered NaxLiyNi0.4Fe0.2Mn0.4O2 intergrowth electrodes for sodium ion batteries, Nano Energy 134 (2025) 110556, https://doi.org/10.1016/j.nanoen.2024.110556.
[7] Y. Xie, E. Gabriel, L. Fan, I. Hwang, X. Li, H. Zhu, Y. Ren, C. Sun, J. Pipkin, M. Dustin, M. Li, Z. Chen, E. Lee, H. Xiong, Role of lithium doping in P2–$Na_{0.67}Ni_{0.33}Mn_{0.67}O_2$ for sodium–ion batteries, Chem. Mater. 33 (2021) 4445–4455, https://doi.org/10.1021/acs.chemmater.1c00569.
[8] S. Yuan, L. Yu, G. Qian, Y. Xie, P. Guo, G. Cui, J. Ma, X. Ren, Z. Xu, S.–J. Lee, J.–S. Lee, Y. Liu, Y. Ren, L. Li, G. Tan, X. Liao, P2–Type moisture–stable and high–voltage–tolerable cathodes for high–energy and long–life sodium–ion batteries, Nano Lett. 23 (2023) 1743–1751, https://doi.org/10.1021/acs.nanolett.2c04465.
[9] Y. Liu, X. Fang, A. Zhang, C. Shen, Q. Liu, H.A. Enaya, C. Zhou, Layered P2–Na2/3[Ni1/3Mn2/3]O2 as high–voltage cathode for sodium–ion batteries: the capacity decay mechanism and Al2O3 surface modification, Nano Energy 27 (2016) 27–34, https://doi.org/10.1016/j.nanoen.2016.06.026.
[10] Z. Xu, K. Song, X. Chang, L. Li, W. Zhang, Y. Xue, J. Zhang, D. Lin, Z. Liu, Q. Wang, Y. Yu, C. Yang, Layered oxide cathodes: a comprehensive review of characteristics, research, and development in lithium and sodium ion batteries, Carbon Neutraliz. 3 (2024) 832–856, https://doi.org/10.1002/cnl2.162.
[11] S. Wu, F. Wu, X. Ye, L. Sheng, H. Zhang, K. Liang, J. Li, Y. Ren, P. Wei, Inhibiting the P2–O2 phase transition of P2–$Na_{0.67}Ni_{0.33}Mn_{0.67}O_2$ via high–valence tungsten doping for sodium–ion batteries, Rare Metals. 44 (2025) 3806–3816, https://doi.org/10.1007/s12598–024–03217–3.
[12] R.D. Shannon, C.T. Prewitt, Effective ionic radii in oxides and fluorides, Acta. Crystallogr B Struct. Sci. 25 (1969) 925–946, https://doi.org/10.1107/S0567740869003220.
[13] H. Taguchi, M. Sonoda, M. Nagao, Effect of Ge4+ion on electrical properties of (La0.1Ca0.9)(Mn1−xGex)O3, J. Solid. State Chem. 140 (1998) 431–434, https://doi.org/10.1006/jssc.1998.7864.
[14] G. Liang, E. Olsson, J. Zou, Z. Wu, J. Li, C. Lu, A.M. D'Angelo, B. Johannessen, L. Thomsen, B. Cowie, V.K. Peterson, Q. Cai, W.K. Pang, Z. Guo, Introducing 4 *s* –2 *p* orbital hybridization to stabilize spinel oxide cathodes for lithium–ion batteries, Angew. Chem. Int. Ed 61 (2022) e202201969, https://doi.org/10.1002/anie.202201969.
[15] C. Wei, W. Yang, L. Wang, M. Wang, Y. Jiao, Z. Wang, B. Li, P. Zhai, Z. Zhao, Y. Gong, Synergistic charge compensation process in P2–type layered oxides enables high–reversibility sodium–ion batteries, Small 21 (2025) 2505429, https://doi.org/10.1002/smll.202505429.
[16] P. Zhou, J. Zhang, Z. Che, Z. Quan, J. Duan, X. Wu, J. Weng, J. Zhao, J. Zhou, Insights into the enhanced structure stability and electrochemical performance of Ti4+/F− co–doped P2–Na0.67Ni0.33Mn0.67O2 cathodes for sodium ion batteries at high voltage, J. Energy Chem. 67 (2022) 655–662, https://doi.org/10.1016/j.jechem.2021.10.032.
[17] Q. Shi, R. Qi, X. Feng, J. Wang, Y. Li, Z. Yao, X. Wang, Q. Li, X. Lu, J. Zhang, Y. Zhao, Niobium–doped layered cathode material for high–power and low–temperature sodium–ion batteries, Nat. Commun. 13 (2022) 3205, https://doi.org/10.1038/s41467–022–30942–z.
[18] X. Zhao, Q. Ruan, P. He, Y. Guo, X. Yan, X. Zhang, B. Liu, H. Chen, J. Fan, Ge–doped LiNi0.6Co0.2Mn0.2O2 cathode material for elevated electrochemical performance of lithium ion batteries, J. Alloys. Compd. 1020 (2025) 179373, https://doi.org/10.1016/j.jallcom.2025.179373.
[19] Y. Zhang, Z. Su, J. Ding, Synthesis and electrochemical properties of Ge–doped Li3V2(PO4)3/C cathode materials for lithium–ion batteries, J. Alloys. Compd. 702 (2017) 427–431, https://doi.org/10.1016/j.jallcom.2017.01.267.
[20] Q. Pei, M. Lu, Z. Liu, D. Li, X. Rao, X. Liu, S. Zhong, Improving the $Na_{0.67}Ni_{0.33}Mn_{0.67}O_2$ cathode material for high–voltage cyclability via Ti/Cu codoping for sodium–ion batteries, ACS. Appl. Energy Mater. 5 (2022) 1953–1962, https://doi.org/10.1021/acsaem.1c03466.
[21] B.H. Toby, R.B. Von Dreele, *GSAS–II* : the genesis of a modern open–source all purpose crystallography software package, J. Appl. Crystallogr. 46 (2013) 544–549, https://doi.org/10.1107/S0021889813003531.
[22] E. Gabriel, Z. Wang, V.V. Singh, K. Graff, J. Liu, C. Koroni, D. Hou, D. Schwartz, C. Li, J. Liu, X. Guo, N.C. Osti, S.P. Ong, H. Xiong, Influence of interlayer cation ordering on Na transport in P2–type $Na_{0.67-x}Li_yNi_{0.33-z}Mn_{0.67+z}O_2$ for sodium–ion batteries, J. Am. Chem. Soc. 146 (2024) 15108–15118, https://doi.org/10.1021/jacs.4c00869.
[23] N. Yabuuchi, R. Hara, M. Kajiyama, K. Kubota, T. Ishigaki, A. Hoshikawa, S. Komaba, New O2/P2–type Li–excess layered manganese oxides as promising multi–functional electrode materials for rechargeable Li/Na batteries, Adv. Energy Mater. 4 (2014) 1301453, https://doi.org/10.1002/aenm.201301453.
[24] A.C. Lazanas, M.I. Prodromidis, Electrochemical impedance spectroscopy–A tutorial, ACS. Meas. Sci. Au 3 (2023) 162–193, https://doi.org/10.1021/acsmeasuresciau.2c00070.
[25] P. Iurilli, C. Brivio, V. Wood, On the use of electrochemical impedance spectroscopy to characterize and model the aging phenomena of lithium–ion batteries: a critical review, J. Power. Sources. 505 (2021) 229860, https://doi.org/10.1016/j.jpowsour.2021.229860.
[26] P.F. Wang, H.R. Yao, X.Y. Liu, Y.X. Yin, J.N. Zhang, Y. Wen, X. Yu, L. Gu, Y.G. Guo, Na+/vacancy disordering promises high–rate Na–ion batteries, Sci. Adv. 4 (2018) eaar6018, https://doi.org/10.1126/sciadv.aar6018.

[27] H.–R. Yao, W.–J. Lv, X.–G. Yuan, Y.–J. Guo, L. Zheng, X.–A. Yang, J. Li, Y. Huang, Z. Huang, P.–F. Wang, Y.–G. Guo, New insights to build Na+/vacancy disordering for high–performance P2–type layered oxide cathodes, Nano Energy 97 (2022) 107207, https://doi.org/10.1016/j.nanoen.2022.107207.
[28] W. Yang, X. Liu, R. Qiao, P. Olalde–Velasco, J.D. Spear, L. Roseguo, J.X. Pepper, Y. Chuang, J.D. Denlinger, Z. Hussain, Key electronic states in lithium battery materials probed by soft X–ray spectroscopy, J. Electron. Spectros. Relat. Phenomena 190 (2013) 64–74, https://doi.org/10.1016/j.elspec.2013.03.008.
[29] W. Yang, T.P. Devereaux, Anionic and cationic redox and interfaces in batteries: advances from soft X–ray absorption spectroscopy to resonant inelastic scattering, J. Power. Sources. 389 (2018) 188–197, https://doi.org/10.1016/j.jpowsour.2018.04.018.
[30] R. Qiao, L.A. Wray, J.–H. Kim, N.P.W. Pieczonka, S.J. Harris, W. Yang, Direct experimental probe of the Ni(II)/Ni(III)/Ni(IV) redox evolution in $LiNi_{0.5}Mn_{1.5}O_4$ electrodes, J. Phys. Chem. C 119 (2015) 27228–27233, https://doi.org/10.1021/acs.jpcc.5b07479.
[31] R. Qiao, Y. Wang, P. Olalde–Velasco, H. Li, Y.–S. Hu, W. Yang, Direct evidence of gradient Mn(II) evolution at charged states in LiNi0.5Mn1.5O4 electrodes with capacity fading, J. Power. Sources. 273 (2015) 1120–1126, https://doi.org/10.1016/j.jpowsour.2014.10.013.
[32] G. Lee, J. Wu, D. Kim, K. Cho, M. Cho, W. Yang, Y. Kang, Reversible anionic redox activities in conventional $LiNi_{1/3}Co_{1/3}Mn_{1/3}O_2$ cathodes, Angew. Chem. Int. Ed 59 (2020) 8681–8688, https://doi.org/10.1002/anie.202001349.
[33] R. Qiao, K. Dai, J. Mao, T.–C. Weng, D. Sokaras, D. Nordlund, X. Song, V. S. Battaglia, Z. Hussain, G. Liu, W. Yang, Revealing and suppressing surface Mn(II) formation of Na0.44MnO2 electrodes for Na–ion batteries, Nano Energy 16 (2015) 186–195, https://doi.org/10.1016/j.nanoen.2015.06.024.
[34] I. Hung, L. Zhou, F. Pourpoint, C.P. Grey, Z. Gan, Isotropic high field NMR spectra of Li–ion battery materials with anisotropy >1 MHz, J. Am. Chem. Soc. 134 (2012) 1898–1901, https://doi.org/10.1021/ja209600m.
[35] Y.–Y. Hu, E.M. Levin, K. Schmidt–Rohr, Broadband "infinite–speed" magic–angle spinning NMR spectroscopy, J. Am. Chem. Soc. 131 (2009) 8390–8391, https://doi.org/10.1021/ja903334p.
[36] J. Hu, Q. Dou, E. Gabriel, D. Hou, K. Graff, R. Schrock, M. Wu, S. Deng, J.A. Russell, C. Koroni, D. Schwartz, A. Zhu, B. Li, Y. Dong, H. Xiong, Single crystalline $Na_{0.67}Ni_{0.33}Mn_{0.67}O_2$ positive electrode material via Molten salt synthesis for sodium ion batteries, ACS. Appl. Energy Mater. 8 (2025) 4941–4947, https://doi.org/10.1021/acsaem.5c00264.
[37] Z. Lu, J.R. Dahn, In situ X–ray diffraction study of P2–Na2/3[Ni1/3Mn2/3]O2, J. Electrochem. Soc. 148 (2001) A1225, https://doi.org/10.1149/1.1407247.
[38] J.W. Somerville, A. Sobkowiak, N. Tapia–Ruiz, J. Billaud, J.G. Lozano, R.A. House, L.C. Gallington, T. Ericsson, L. Häggström, M.R. Roberts, U. Maitra, P.G. Bruce, Nature of the "Z"–phase in layered Na–ion battery cathodes, Energy Environ. Sci. 12 (2019) 2223–2232, https://doi.org/10.1039/C8EE02991A.
[39] J. Hong, W.E. Gent, P. Xiao, K. Lim, D.–H. Seo, J. Wu, P.M. Csernica, C.J. Takacs, D. Nordlund, C.–J. Sun, K.H. Stone, D. Passarello, W. Yang, D. Prendergast, G. Ceder, M.F. Toney, W.C. Chueh, Metal–oxygen decoordination stabilizes anion redox in Li–rich oxides, Nature Mater 18 (2019) 256–265, https://doi.org/10.1038/s41563–018–0276–1.
[40] W. Tian, W. Zeng, T. Wang, J. Tian, D. Yuan, J. Wang, S. Mu, Ge–regulated ordered phase in pseudosphere–structured $LiNi_{0.5}Mn_{1.5}O_4$ spinel effectively inhibits Mn dissolution, Inorg. Chem. 62 (2023) 12079–12088, https://doi.org/10.1021/acs.inorgchem.3c01596.